PHYSICAL REVIEW A **70**, 032710 (2004)

Semiclassical complex angular momentum theory and Padé reconstruction for resonances, rainbows, and reaction thresholds

D. Sokolovski[1] and A. Z. Msezane[2]

[1]*School of Mathematics and Physics, Queen's University of Belfast, Belfast, BT7 1NN, United Kingdom*

[2]*Department of Physics and Center for Theoretical Studies of Physical Systems, Clark Atlanta University, Atlanta, Georgia 30314, USA*

(Received 26 November 2003; published 23 September 2004)

A semiclassical complex angular momentum theory, used to analyze atom-diatom reactive angular distributions, is applied to several well-known potential (one-particle) problems. Examples include resonance scattering, rainbow scattering, and the Eckart threshold model. Padé reconstruction of the corresponding matrix elements from the values at physical (integral) angular momenta and properties of the Padé approximants are discussed in detail.

DOI: 10.1103/PhysRevA.70.032710 PACS number(s): 34.50.Lf, 34.50.Pi

I. INTRODUCTION

Following Ref. [1], there has been renewed interest in the semiclassical description of reactive systems consisting of three or more atoms [2–4]. Although it is difficult to obtain accurate atom-diatom S-matrix elements using semiclassical techniques, an *a posteriori* semiclassical analysis is possible once the S matrix has been computed, e.g., in coupled-channel [5] or time-dependent [6] calculations. In this vein, a semiclassical complex angular momentum (CAM) method for analyzing reactive differential cross sections (DCS's) has been developed and applied to a wide range of atom-diatom systems in Refs. [7–15]. In the CAM approach, the scattering amplitude is decomposed into subamplitudes describing capture into a number of Regge states and the remnant "optical" term, often containing contributions from direct reactive trajectories. The method requires therefore the knowledge of the analytical properties of an S-matrix element, and relies on the Padé reconstruction [16] in the CAM plane. Some aspects of the Padé reconstruction have been discussed in Ref. [12]. The success, or otherwise, of such semiclassical analysis depends on the complexity of the scattering system and the accuracy with which the scattering data have been computed. It is desirable, for this reason, to test the method on a number of well-studied benchmark cases, as will be done below. Further information about the application of the CAM approach to potential scattering can be found in Refs. [17] and [18]. The purpose of this paper is thus threefold: first, to give clear illustrations for the use of the CAM approach employed in Refs. [9–15]. Second, to investigate the properties of the Padé method for the cases when analytical properties of the S matrix are known in advance. And, third, to provide where possible, a further insight into the physics of well-studied scattering phenomena, such as rainbows and forward glories. The rest of the paper is organized as follows: in Sec. II we briefly outline our CAM approach for central scattering problems. Section III describes semiclassical evaluation of the "unfolded" scattering amplitude. In Sec. IV the theory is applied to a single scattering resonance and the analytical properties of the corresponding Padé approximant are studied in some detail. In Sec. V, the CAM approach is applied to a model designed to mimic a reactive scattering system. A generic type of angular distributions encountered in atom-diatom reactions as well as the success of the quadratic approximation for the potential phase [9] are explained. In Sec. VI the theory is applied to the rainbow scattering off a rectangular potential well with a refraction index close to that of water. Section VII analyzes the Eckart threshold model recently used to explain time-delayed forward scattering in the $H+D_2 \rightarrow HD+D$ reaction [15]. Section VIII contains our conclusions and discussion.

II. SEMICLASSICAL UNFOLDING OF THE SCATTERING AMPLITUDE

The theory of this section closely follows a similar approach developed in Refs. [9–11] and [14] for reactive atom-diatom collisions. For a particle scattered by a central field $V(r)$, the differential cross section (DCS) $\sigma(\theta)$,

$$\sigma(\theta) = |f(\theta)|^2, \tag{1}$$

can be obtained from the partial wave sum (PWS) for the scattering amplitude $f(\theta)$,

$$f(\theta) = (2ik)^{-1}\sum_{J=0}^{\infty}(2J+1)P_J[\cos(\theta)](S^J - 1), \tag{2}$$

where k, J, θ, $P_J[\cos(\theta)]$, and S^J are the wave vector, the angular momentum quantum number, the scattering angle, a Legendre polynomial of degree J, and the scattering matrix element, respectively. For large J and $1/J < \theta < \pi - 1/J$, $P_J[\cos(\theta)]$ can be written as a sum of two traveling-wave components [18,19],

$$P_J \approx P_J^+ + P_J^-, \tag{3}$$

$$P_J^{\pm} \equiv [1/2\pi\lambda\ \sin(\theta)]^{1/2}\exp[\pm i(\lambda\theta - \pi/4)]. \tag{4}$$

As usual, in the semiclassical analysis [19] we can use

$$\sum_{J=0}^{\infty}(J+1/2)P_J(\cos\,\theta)=\delta(1-\cos\,\theta), \tag{5}$$

to replace in Eq. (2) S^J-1 by S^J for any $\theta\neq 0$. Inserting Eq. (3) into Eq. (2) and applying the Poisson sum formula [19,20] we obtain a representation for the scattering amplitude[19,9] $[S^J=S(J+1/2)]$

$$f(\theta)=(1/ik)(2\pi\,\sin\,\theta)^{-1/2}\sum_{m=-\infty}^{\infty}(-1)^m \times\int_0^{\infty}d\lambda\lambda^{1/2}S(\lambda)\{\exp[i\lambda(\theta+2m\pi)-i\pi/4] + \exp[-i\lambda(\theta-2m\pi)+i\pi/4]\}, \tag{6}$$

valid for a semiclassical collision dominated by large angular momenta excluding small vicinities of the forward ($\theta=0$) and backward ($\theta=\pi$) scattering angles. Now it is convenient to rewrite Eq. (6) in an equivalent form,

$$f(\theta)=(ik)^{-1}[2\pi\,\sin(\theta)]^{-1/2}\sum_{m=-\infty}^{\infty}\tilde{f}(\varphi_m)\exp(-i\pi/4-im\pi/2), \tag{7}$$

where

$$\varphi_m(\theta)\equiv(-1)^{m+1}\theta+\pi[m+1/2+(-1)^m/2], \quad m=\cdots-1,0,1\cdots \tag{8}$$

and

$$\tilde{f}(\varphi)\equiv\int_0^{\infty}\exp(i\lambda\varphi)S(\lambda)\lambda^{1/2}d\lambda, \quad -\infty\geqslant\varphi\leqslant\infty. \tag{9}$$

It can now be seen [9] that φ can be interpreted as the angle by which the position vector $\vec{r}$ of the particle rotates in the course of collision around the direction of the angular momentum, φ_m give all values of φ consistent with the scattering angle θ, and the scattering amplitude can be found by summing (with appropriate phases) $\tilde{f}(\varphi)$ over all φ_m. The summation can be seen as "folding" $\tilde{f}(\varphi)$ into a finite interval $[0,\pi]$ and we refer to $\tilde{f}$ as an "unfolded" scattering amplitude. Semiclassically, $\vec{r}$ rotates in the positive direction around the angular momentum vector $\vec{J}$ and we expect the $m\geqslant 0$ terms to dominate the sum in Eq. (7). Among these we will distinguish the *nearside* terms with $m=0,2,4\ldots$ and *farside* terms with $m=1,3,5\ldots$, respectively. Finally, note that the geometrical factor $(\sin\,\theta)^{1/2}$ has been removed from $\tilde{f}(\varphi)$ for convenience.

III. UNFOLDED SCATTERING AMPLITUDE

The unfolded amplitude $\tilde{f}(\varphi)$ contains contributions from various direct and resonance processes which determine the shape of the DCS, Eq. (1), and we will briefly discuss its properties next. In the semiclassical limit, the integral (6) can be evaluated by the stationary phase method, provided the phase shift $\delta(\lambda)$,

$$S(E,\lambda)=\exp[i\delta(E,\lambda)], \quad \lambda\equiv J+1/2, \tag{10}$$

is a slowly varying function of λ, $|\delta(E,\lambda+1)-\delta(E,\lambda)|\ll 1$. For a given energy E (we will omit the energy dependence of S), $S(\lambda)$ may have poles λ_n, $n=0,1,2\ldots$ in the first quadrant of the complex λ plane. In the single-channel case considered here, any such pole is complemented by a complex conjugate zero, λ_n^* [21], so that a pole-zero pair contributes to $\delta(\lambda)$ a term $-i\,\ln[(\lambda-\lambda_n^*)/(\lambda-\lambda_n)]$. For a resonance pole located close to the real λ axis, this contribution rapidly varies with λ and, to find the semiclassical asymptote for $\tilde{f}(\varphi)$, it is convenient to write

$$S(\lambda)=\prod_{n=0}^{N_{res}}\frac{(\lambda-\lambda_n^*)}{(\lambda-\lambda_n)}\exp[i\phi(\lambda)], \tag{11}$$

where $\phi(\lambda)$ is the slowly varying "potential" phase and N_{res} is the number of resonance poles. Equivalently, $S(\lambda)$ can be written as a sum of pole terms,

$$S(\lambda)=\sum_{n=0}^{N_{res}}\frac{\rho_n}{(\lambda-\lambda_n)}\exp[i\phi(\lambda)]. \tag{12}$$

with the quantities ρ_n given by

$$\rho_n\equiv 2i\,\mathrm{Im}\,\lambda_n\prod_{j\neq n}\frac{(\lambda_n-\lambda_j^*)}{(\lambda_n-\lambda_j)}. \tag{13}$$

The expression, Eq. (6), for $\tilde{f}(\varphi)$ thereby reduces to a sum of oscillatory integrals of the form

$$\int\frac{g(\lambda)}{(\lambda-\lambda_n)}\exp[i\phi(\lambda)+i\lambda\varphi]d\lambda, \tag{14}$$

where $g(\lambda)\equiv\lambda^{1/2}$ is a slowly varying function away from the origin, the denominator has a pole in the first quadrant of the complex λ plane, and $\exp[i\phi(\lambda)]$ oscillates rapidly. Asymptotic approximations for such integrals are well known (see, for example, Ref. [22]) and are discussed in detail in Appendix B of Ref. [8]. Typically, they contain three contributions [see Eq. (B15) of Ref. [8]], and combining those corresponding to the stationary point results for the expression (14) yields the direct, or "optical," part of $\tilde{f}(\varphi)$,

$$\tilde{f}^{opt}(\varphi)\equiv\left\{\frac{2\pi}{-\phi_{\lambda\lambda}(\lambda_s)}\right\}^{1/2}\prod_{n=0}^{N_{res}}\frac{(\lambda_s-\lambda_n^*)}{(\lambda_s-\lambda_n)} \times\exp[i\phi(\lambda_s)+i\lambda_s\phi-i\pi/4], \tag{15}$$

where the classical value of λ corresponding to the rotation angle φ is given by the stationary phase condition

$$\phi_\lambda(\lambda_s)=-\varphi \tag{16}$$

and a subscript(s) λ denote(s) differentiation with respect to λ. Equation (15) implies that a single trajectory leads to a given angle φ and yields the primitive semiclassical approximation to the unfolded amplitude. Note that it differs, in general, from the usual Ford-Wheeler result [18] in that only

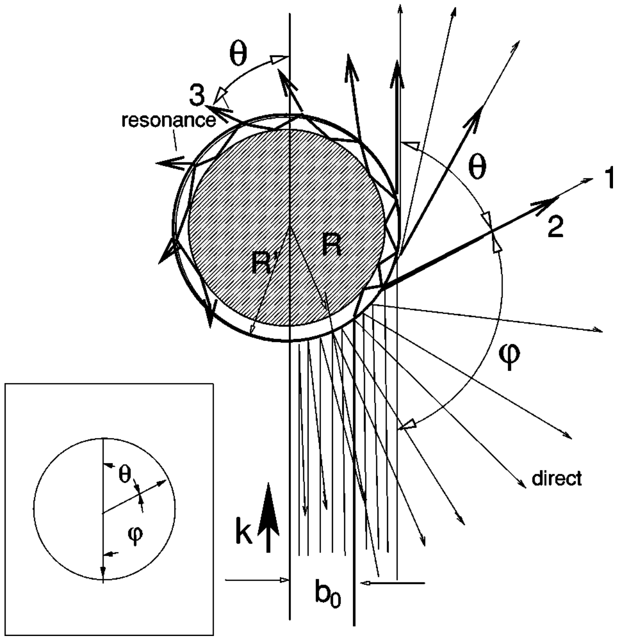

FIG. 1. Schematic diagram showing particles with wave vector k scattered off a penetrable layer surrounding a hard-sphere potential. Most trajectories bounce off the outer layer (thin solid), while the particle with the impact parameter close to b_0 can penetrate the barrier and continue propagating around the hard core as it decays into the outer region (thick solid). One direct (1) and two resonant (2, 3) pathways lead to the same scattering angle θ. Inset: relation between the scattering angle θ and the rotation angle φ.

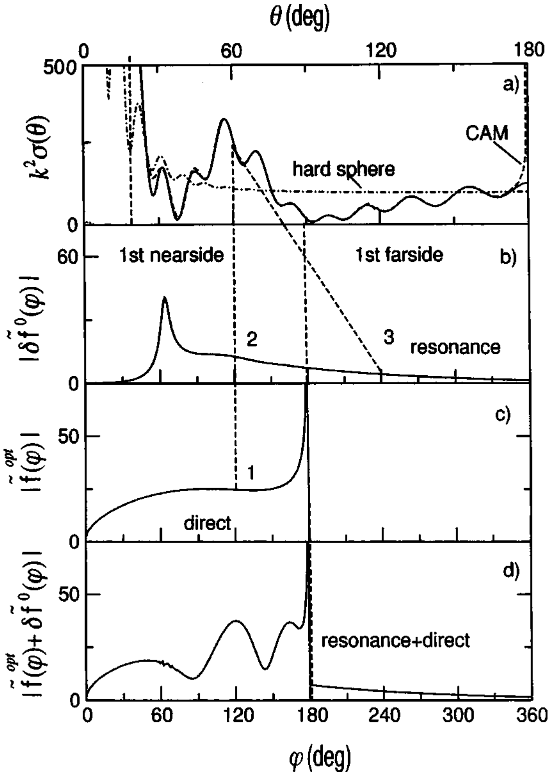

FIG. 2. (a) DCS for the model in Fig. 1 with $kR'=20$, $kd=3.5$, and $\Omega R'=3$: exact (solid) and obtained by the CAM approach (dashed). Also shown for comparison is the DCS (dot-dashed) for an impenetrable sphere with a radius equal to that of the outer potential layer; (b) first nearside and farside components of the LCF $\widetilde{\delta f}^0(\varphi)$ for the above model; (c) the direct component $\tilde{f}^{opt}(\varphi)$ for the above model (ignoring the diffraction effects of the outer layer); (d) coherent sum of $\tilde{f}^{opt}(\varphi)$ and $\widetilde{\delta f}^0(\varphi)$.

the smooth part of the phase, $\phi(\lambda)$, rather than the full phase shift $\delta(\lambda)$ is used to determine λ_s. The two expressions agree, however, in the absence of resonance poles ($N_{res}=0$).

For a resonance pole at λ_n, we combine the two remaining terms in Eq. (B.15) of Ref. [8] into a correction term $\widetilde{\delta f}^n(\varphi)$,

$$\widetilde{\delta f}^n(\varphi) \equiv -i\pi\rho_n erfc(u_n)\exp[i\phi(\lambda_n)+i\lambda_n\varphi] + \pi^{1/2}\rho_n u_n^{-1}\exp[i\phi(\lambda_s)+i\lambda_s\varphi], \qquad (17)$$

where

$$u_n \equiv [\phi(\lambda_s)-\phi(\lambda_n)+(\lambda_s-\lambda_n)\varphi]^{1/2} \qquad (18)$$

and $\mathrm{erfc}(z)\equiv 2\pi^{-1/2}\int_z^\infty \exp(-t^2)dt$ is the complementary error function [23]. The lifetime correction function (LCF), $\widetilde{\delta f}^n(\varphi)$, has a simple physical meaning. Consider a repulsive collision such that $\lambda_s(\varphi)$ increases with φ, i.e., the higher angular momenta correspond to smaller scattering angles, $\theta=\pi-\varphi$. Let

$$\varphi_{res} \equiv \varphi(\mathrm{Re}(\lambda_n))$$

be the angle corresponding to the direct trajectory with the angular momentum equal to real part of the nth Regge pole position. Then for $\varphi<\varphi_{res}$ [cf. Eqs. (B16) and (B17) of Ref. [8]] $\widetilde{\delta f}^n$ vanishes, while for $\varphi \gg \varphi_{res}$ it reduces to a single exponential term [cf. Eq. (B18) of Ref. [7]]

$$\widetilde{\delta f}^n(\varphi) \approx 2\pi\rho_n \exp[i\phi(\lambda_n)]\exp(i\varphi \mathrm{Re}\lambda_n - \varphi\, \mathrm{Im}\,\lambda_n). \qquad (19)$$

It is seen therefore that $\widetilde{\delta f}^n$ describes exponential angular decay of a resonance Regge state which is formed for $\lambda \approx \mathrm{Re}\lambda_n$, i.e., the metastable state of a particle rotating in the positive direction around the direction of the total angular momentum (see Refs. [9,10], and the discussion in Sec. IV below). For a pole with a shorter angular life $\Delta\varphi$, $\Delta\varphi \equiv 1/(2\mathrm{Im}\lambda_n)$, the LCF may have no pronounced exponential tail but would still describe the effect of capture in the corresponding Regge state [15]. Finally, if several resonance poles are present, the unfolded amplitude is a coherent sum of the optical and several (N_{res}) correction terms,

$$\tilde{f}(\varphi) \approx \tilde{f}^{opt}(\varphi) + \sum_{n=0}^{N_{res}} \widetilde{\delta f}^n(\varphi). \qquad (20)$$

"Folding" $\tilde{f}$ into the interval $0,\theta<\pi$ as in Eq. (7) allows us to relate the structure observed in the angular distributions to interference between various resonance and direct pathways leading to the scattering angle θ. Next we apply this approach to an isolated potential resonance.

IV. SINGLE RESONANCE AND ITS PADÉ RECONSTRUCTION

We consider a simple model which provides an illustration for the application of CAM method described above as well as a benchmark case for the study of more complex systems. This consists of a flux of particles with a wave vector k scattered off a hard-sphere potential of a radius R augmented by a thin semitransparent spherical layer of radius $R' = R + d$,

$$V(r) = \infty, \text{ for } r < R \text{ and } V(r) = \Omega\delta(R + d) \text{ for } r > R,$$

where $\Omega\delta(z)$ is the Dirac δ function of magnitude Ω. In the semiclassical limit, $kR' \gg 1$, [note that kR' is approximately the number of partial waves needed to converge the PWS in Eq. (2)] the scattering can be described as follows. For a large Ω, the potential well between the outer layer and the hard core supports a number of energy levels. Most of the trajectories incident on the $V(r)$ are reflected off the outer layer as if it were impenetrable. However, a particle with an impact parameter b_0 (angular momentum $\hbar k b_0$) such that, when it impacts on the outer shell, the energy of its radial motion is close to that of a level in the well, may penetrate the barrier. It will then initiate a wave (Regge state) which creeps around the hard core while leaking into the outer region, Fig. 1, The angular distance traveled by the wave (life angle or angular life) $\Delta\varphi$ depends on the transparency of the barrier determined by the Ω. As shown in Fig. 1, for $\Delta\varphi < 2\pi$ and $\theta > \varphi_{res}$ there are three pathways leading to scattering into θ: (i) directly off the outer potential layer (first nearside direct), (ii) via capture in the Regge state and subsequent decay at $\varphi = \pi - \theta$ (first nearside resonance), and (iii) via capture in the Regge state and subsequent decay at $\varphi = \pi + \theta$ (first farside resonance). A resonance with a larger lifeangle could result in a larger number of resonance pathways, and interference between them would determine the shape of the corresponding DCS.

The S-matrix element for the potential in Eq. (21) is easily evaluated by requiring that the radial wave function vanish at $r = R$ and has a discontinuity in the logarithmic derivative at $r = R'$,

$$S(k,\lambda) = -\frac{4H_\lambda^2(kR) + \pi\Omega R'[H_\lambda^1(kR)H_\lambda^2(kR') - H_\lambda^2(kR)H_\lambda^1(kR')]H_\lambda^2(kR')}{4H_\lambda^1(kR) + \pi\Omega R'[H_\lambda^1(kR)H_\lambda^2(kR') - H_\lambda^2(kR)H_\lambda^1(kR')]H_\lambda^1(kR')}, \tag{21}$$

where $H_\lambda^{1(2)}(z)$ are the Hankel functions of the first (second) kind [23]. The exact DCS for $kR' = 20$, $kd = 3.5$, and $\Omega R' = 3$ obtained by the partial wave summation up to $J = 39$ is shown in Fig. 2(a). In the middle of the angular range, it shows a pronounced structure whose origin we seek to explain. We note first that for a pure hard-sphere potential the DCS in this region has nearly constant value of $\approx R'^2/4 = 100$ so that the pattern must be related to the presence of a resonance.

Consider the analytical properties of $S(\lambda)$ in Eq. (21). For $\Omega = 0$ and $\Omega \to \infty$, the matrix element reduces to that for a hard-sphere potential of the radii R and $R + d$, respectively. In the complex λ plane, $S(\lambda)$ has poles associated with the zeroes of the denominator in Eq. (21). For Ω large but finite, these fall into two categories: poles associated with an infinite number of zeroes of $H_\lambda^1(kR')$ which are slightly perturbed by the presence of the $4H_\lambda^1(kR)$ term, and the pole associated with the zero of the expression in the square bracket. The poles of the first kind are the diffraction poles responsible for the diffraction effect in scattering off the outer sphere [20], and we will not discuss them further in this work. The pole of the second kind is the resonance pole of interest responsible for trapping the penetrated wave between the outer and inner spheres. It is readily seen that in Eq. (21) the expression in the square brackets is the value of the regular radial wave function at $r = R' = R + d$ and the condition that it vanishes gives the position of a bound state which exists for $\Omega \to \infty$. Due to the presence of the $4H_\lambda^1(kR)$ term the corresponding pole acquires an imaginary part, typically, of order Ω^{-1} so that it describes a metastable, rather than a bound state.

Given the analytic form of the S matrix, it is a relatively simple matter to calculate both the pole positions and the corresponding residues. In numerical modeling of realistic chemical reactions no simple analytic form is available for the S-matrix element and one has to rely on numerical analytic continuation of the scattering data computed for physical integer values of J (half-integer values of λ) [7]. In order to study the properties and accuracy of such continuation, we will construct for our model a diagonal $[K/K]$ Padé approximant [9,10,15,16],

$$S^{Pade}(\lambda) = C\prod_{j=1}^{K}\frac{(\lambda - \xi_j)}{(\lambda - \lambda_j)}\exp[i\Phi(\lambda)] \tag{22}$$

using $2K+1$ values of $S(J+1/2)$, $J = 0, 1, 2, \ldots, 2K$ to determine pole positions λ_j, zero positions ξ_j and the constant C [12,16]. Note that in Eq. (22) the data have been "preconditioned" by extracting a rapidly oscillating phase $\Phi(\lambda)$,

$$\Phi(\lambda) \equiv -\pi/2K(\lambda - 1/2)^2 + \pi(\lambda - 1/2), \tag{23}$$

in order to improve accuracy of the Padé method [12]. The poles and zeroes of the Padé approximant are, in general, not the same as the true poles of the S matrix in Eq. (11). However, at least some of the true poles must be reproduced correctly and we will use Eq. (22) to obtain their positions and residues. Note also that the phase $\Phi(\lambda)$ is different from

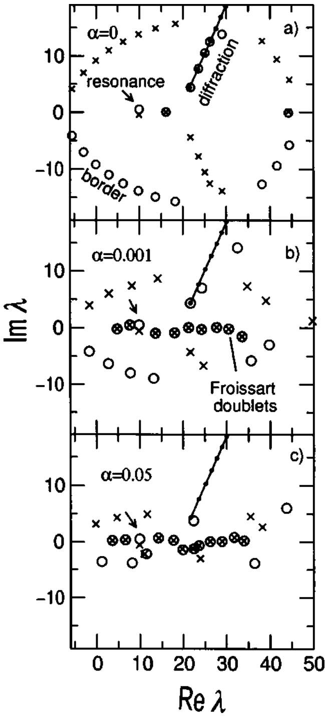

FIG. 3. Poles (circles) and zeroes (crosses) obtained by Padé reconstruction for the model in Fig. 1 with $kR=20$, $kd=3.5$, and $\Omega R'=3$: (a) with no extra noise; (b) with extra noise of 0.1%, ($\alpha=0.001$); (c) with more noise ($\alpha=0.05$). Also shown (joined closed circles) are exact diffraction poles.

the potential phase $\phi(\lambda)$ in Eq. (11), which can, however, be easily calculated once the Padé approximant has been obtained.

For the system Eq. (21) the pole /zero structure resulting from such reconstruction for $kR'=20$, $kd=3.5$, $\Omega R'=3$, and $K=19$ is shown in Fig. 3. The Padé approximant has at its disposal 19 poles and one might expect it to correctly reproduce the resonance pole and the first 18 of the diffraction poles sequence [20,24] starting at $\lambda \approx kR=20$. Remarkably, this is not what happens. As shown in Fig. 3(a), only the resonance pole with $\mathrm{Re}\lambda_0 \approx 10.4+0.5i$ and the first four of the diffraction poles are reproduced correctly. The 14 remaining poles, together with the complex zeroes, form an oval "boundary," beyond which the Padé approximation fails. Its failure is obvious since the diffraction poles with $n>5$ are absent, and can also be verified by plotting $S(\lambda)$ along a given direction in the complex plane. The size of the boundary is determined by the accuracy (in this case, the machine accuracy) to which the analytic function $S(\lambda)$ is computed. This is further illustrated by adding to the input values $S(J+1/2)$ a random noise,

$$S(J+1/2) \to S(J+1/2) + \alpha[z_1(J) + iz_2(J)], \qquad (24)$$

where z_1 and z_2 are real random variables taking values between $-1/2$ and $1/2$. For the data contaminated with noise ($\alpha=0.001$) the border shrinks, the number of correctly reproduced diffraction poles reduces to two and more poles and zeroes form Froissart doublets (pole-zero pairs mimicking high-frequency noise of the modeled function [16]) in the vicinity of the real axis. For $\alpha=0.05$, i.e., the error of about 5% expected to be present in realistic reactive scattering calculations, the border disintegrates into a loose collection of spurious poles and zeroes with only the resonance and the first diffraction poles reproduced with some accuracy. Importantly for our analysis, the resonance pole position and residue given in Table I are not sensitive to low noise levels and we can continue with the analysis of the DCS with either set of data.

TABLE I. The resonance pole position λ_0 and the residue $r_0 = \exp[i\phi(\lambda_0)]\rho_0$ as function of the noise parameter α for the model in Sec. IV with $kR'=20$, $kd=3.5$, and $\Omega R'=3$.

kR'	α	Reλ	Imλ	Rer_0	Imr_0
20	0.0	10.3924	0.5043	0.6262	0.2254
	0.001	10.3884	0.5046	0.6289	0.2336
	0.05	10.3920	0.5394	0.1416	0.0040

We choose, however, $\alpha=0$ and obtain the parameters required in Eqs. (15) and (17) from the Padé approximant Eq. (22). Figure 4(b) shows the deflection function (solid)

$$\theta(\lambda) = \pi - \phi_\lambda(\lambda_s), \qquad (25)$$

which yields the direct scattering angle for an angular momentum λ, as well as the derivative of the full phase of the S-matrix element, $\mathrm{Arg}\{S(\lambda)\}_\lambda$ (dashed). While the former is essentially that for a hard sphere of radius R', the latter con-

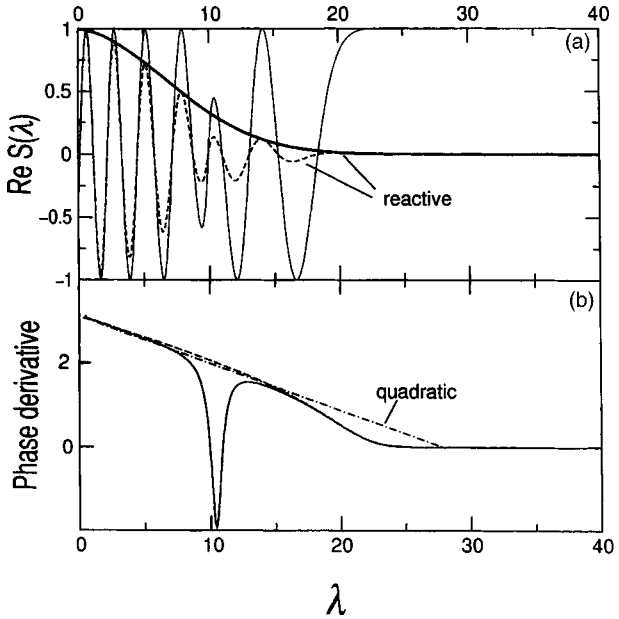

FIG. 4. (a) Real part of the S-matrix element (solid) for the model in Fig. 2 with $kR'=20$ $kd=3.5$, and $\Omega R'=3$. Also shown are the real part (dashed) and modulus (solid) of the "reactive" matrix element obtained by Gaussian truncation Eq. (26); (b) derivative of the phase of the same S-matrix element (solid), the smooth deflection function (dashed), and the linear deflection function resulting from quadratic approximation Eq. (28) (dot-dashed) for the phase.

tains a sharp dip associated with the resonance pole in Table I. (It is this dip which prevents us from using $\pi - \mathrm{Arg}\{S(\lambda)\}_\lambda$ itself as a deflection function.) Various components of the unfolded amplitude $\tilde{f}(\varphi)$ are given in Figs. 2(b) and 2(c). Figure 2(b) shows the formation, at $\varphi_{res} \approx 60°$, and subsequent angular decay of the creeping wave trapped between the outer and inner spheres. The angular life of the corresponding Regge state is $\Delta\varphi = 57° < \pi$ and there are only the first nearside and farside resonance pathways [labeled 2 and 3 in Figs. 1 and 2(b)] leading to an angle $\theta > \pi - \varphi_{res}$. Figure 2(c) shows $\tilde{f}^{opt}(\varphi)$ resulting from direct scattering off the outer sphere and valid for $\varphi < 140°$, beyond which the scattering amplitude is dominated by diffraction not accounted for in our analysis. A coherent sum of the direct optical and resonance components is plotted in Fig. 2(d). We therefore have the following explanation for the DCS in Fig. 2(a). For $\theta > \pi - \varphi_{res}$, it is dominated by direct scattering off the outer potential sphere, with small oscillation arising from interference with the first nearside decay of the resonance wave creeping around the inner hard core. For $40° < \theta < \pi - \varphi_{res} \approx 120°$ the slow oscillations of the DCS result from interference between the nearside decay of the creeping wave and the nearside scattering off the outer potential sphere [cf. Fig. 2(d)], while the small oscillations superimposed on the structure are due to interference with farside decay of the wave. For $\theta < 40°$ our model needs to be modified to include the Regge states (surface waves) associated with diffraction on the outer sphere. Outside this region the full semiclassical result plotted in Fig. 2(a) (dashed) reproduces the exact DCS to the graphical accuracy.

V. REACTIVE SCATTERING RESONANCES AND THE QUADRATIC APPROXIMATION FOR THE POTENTIAL PHASE

As mentioned in the Introduction, the CAM approach has been developed for applications in atom-diatom reactions theory. We can modify the model of the previous section to mimic reactive scattering if we multiply the S-matrix element Eq. (21) by the probability amplitude for reaction to take place at a given total angular momentum,

$$S^{react}(\lambda) = T(\lambda)S(\lambda). \tag{26}$$

To simulate a resonance reaction, the factor $T(\lambda)$ must be chosen so as to make the reaction probability rapidly decrease for large angular momenta (impact parameters) of the collision partners, yet to retain a sufficient amplitude for capture in the resonance Regge state at $\mathrm{Re}\lambda_0 \approx 10.4$,

$$T(\lambda) = \exp(-\lambda^2/\Delta\lambda^2). \tag{27}$$

Physically, the exponential cutoff Eq. (27) results in suppression of direct scattering in the mid-angle range, as well as quenching of the small angle diffraction effects associated with large impact parameters. Mathematically, it means that we can replace the potential phase $\phi(\lambda)$ by its Taylor expansion around $\lambda = 0$ up to quadratic terms (linear approximation is insufficient, as all angular momenta would be scattered into a single angle θ)

$$\phi(\lambda) \approx a\lambda^2 + b\lambda + c, \quad a < 0. \tag{28}$$

The deflection function in Fig. 4(b) is almost linear for $\lambda < 10$ and only shows some curvature for $\lambda > 15$ where reactivity is negligible. Approximation Eq. (28), widely used in atom-diatom reactive scattering [9–15], simplifies Eqs. (15)–(17) and now for the angular momentum leading to a rotation angle φ (scattering angle θ) we have

$$\lambda_s = (\varphi + b)/2|a| = (\pi + b - \theta)/2|a|, \tag{29}$$

the variable u_0 in Eq. (18) becomes (cf. the Appendix of Ref. [8])

$$u_0 = \exp(i\pi/4)|a|^{1/2}(\lambda_0 - \lambda_s), \tag{30}$$

and the LCF $\delta\tilde{f}^0(\varphi)$ is reduced to the difference between the error function term and the primitive semiclassical approximation for the corresponding pole term in Eq. (17),

$$\delta\tilde{f}^0(\varphi) = \lambda_m^{1/2}\rho_m\{i\pi \exp[i\phi(\lambda_0)]\mathrm{erfc}[\exp(-i\pi/4)|a|^{1/2}(\lambda_0 - \lambda_s)] - \pi^{1/2}|a|^{-1/2}(\lambda_s - \lambda_0)^{-1}\exp[i\Phi(\lambda_s) - i\pi/4]\}, \tag{31}$$

where $\Phi(\lambda) \equiv \phi(\lambda) + \lambda\varphi$.

We have repeated the analysis of the previous section for the "reactive" model Eq. (26) with $\Delta\lambda = 10$, $\alpha = 0$ (no extra noise), and other parameters chosen as in Sec. IV. Since the exponential cutoff function Eq. (27) has no poles, we found the pole /zero structure very similar and the deflection function identical to those shown in Fig. 3(b). The resonance contribution in Fig. 5(b) is also similar to that shown in Fig. 2(b), however, reduced in magnitude (note the difference in scales of the two figures). The optical part in Fig. 5(c) is reduced by the cutoff and vanishes for $\varphi > 140°$. A coherent sum of the two components, Fig. 5(d) follows the curve in Fig. 5(c) up to $\varphi \approx 60°$, shows an interference minimum at $\varphi \approx 85°$, and for larger angles coincides with the resonance term in Fig. 5(b). Accordingly, the DCS in Fig. 5(a) has two distinct parts. For $\theta < 80°$, only two resonance pathways (labeled 2 and 3 in Fig. 5) are available and the oscillatory pattern observed in this region is due to nearside-farside interference of resonance decay with itself. For $\theta > 110°$, the shape of the DCS is determined by direct scattering off the outer potential with small oscillations superimposed on it due to the farside decay of the Regge state. For $80° < \theta < 110°$, the DCS is very small because of destructive interference between the nearside direct and resonance components, seen in Fig. 5(d). Angular distributions of this type have been obtained for the $\mathrm{Cl} + \mathrm{HCl} \rightarrow \mathrm{ClH} + \mathrm{Cl}$ [7,8], $\mathrm{I} + \mathrm{HI} \rightarrow \mathrm{IH} + \mathrm{I}$ [16,14], and $\mathrm{F} + \mathrm{H}_2 \rightarrow \mathrm{FH} + \mathrm{H}$ [11] reactive systems. Our simple model also suggests an explanation for the success of the quadratic phase approximation applied to atom-diatom reactive systems [9–15]. It appears that for such systems the reaction probability, $P(\lambda) = |S(\lambda)|^2$, effectively restricts the reactants angular momenta to the range where the deflection function can be considered linear (and the phase quadratic) and suppresses higher impact parameters for which the deviation from the quadratic model may be considerable.

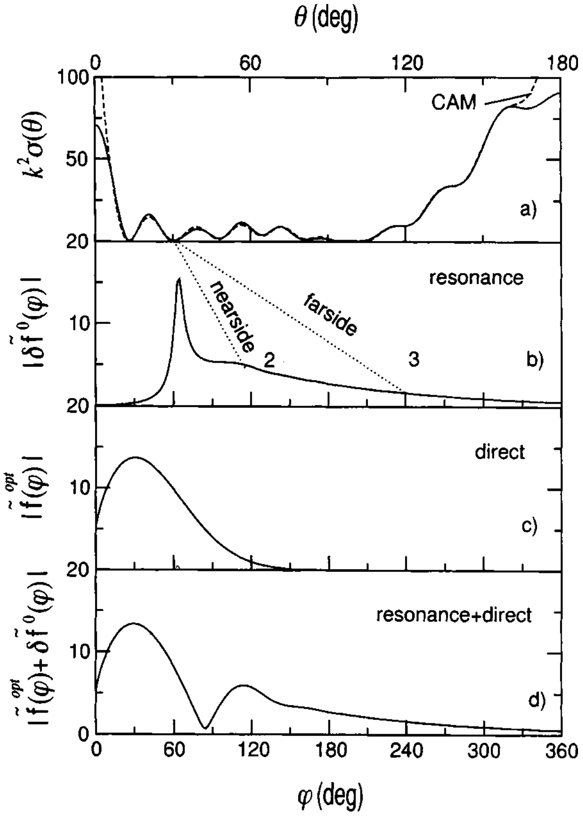

FIG. 5. The same as Fig. 2 but for a reactive S-matrix element Eq. (26) with Gaussian truncation $\Delta\lambda=10$.

VI. SEVERAL RESONANCES: AN OPTICAL RAINBOW

The CAM analysis can be applied in cases when a particular structure in an angular distribution results from interference between decays of many, rather than just one, Regge states. One such example is the rainbow effect observed in scattering of particles (or electromagnetic waves) with a wave vector k from a large ($kR \gg 1$) spherical potential well,

$$V(r) = -V_0 \text{ for } r < R \text{ and 0 otherwise}. \tag{32}$$

The rainbow effect has been studied in great detail. For a systematic analysis we refer the reader to Refs. [20] and [24], and references therein. The *primary rainbow* [24] is usually explained in terms of classical trajectories (rays) which penetrate the interior of the potential and are scattered, after one internal reflection, into the first farside zone. The dependence of the rotation angle φ on the impact parameter b (angular momentum λ) is such that, for φ less that some φ_r, $2\pi < \varphi_r < \pi$, there exist two trajectories with different values of b (λ), while for $\varphi > \varphi_r$ no such trajectories can be found. As a result, the corresponding DCS exhibits an Airy function structure with the main Airy peak at $\theta_r \approx \varphi_r - \pi$ and the shadow (classically forbidden) region at $\theta < \theta_r$. The *secondary rainbow* [24] has a similar explanation in terms of paths experiencing two internal reflections from the potential edge and ending up in the second nearside zone.

The full DCS is shown in Fig. 6(a) by the thin solid line. For $\theta < 90°$, it contains a large forward scattering peak which we will not discuss further. The rainbow part of the cross section occupies the region $\theta > 120°$ where it contains several narrowly spaced peaks. Replacing the Legendre polynomials in the PWS Eq. (2) by their traveling-wave components, $P_J^+(\theta)$ and $P_J^-(\theta)$, we decompose the DCS into the nearside (thick dashed) and farside (thick solid) parts, respectively. It is readily seen that the farside term contains the first three oscillations of the Airy function, and that the high-frequency structure results from nearside-farside interference between the two components. While the description of the rainbow scattering in terms of classical paths is, without a doubt, most natural, it requires the knowledge of the trajectories as well as the phases associated with each of them. For a realistic atom-diatom system such information may not be available, although the value of the S-matrix element can be computed to high accuracy using, for example, a coupled channels method. It is useful therefore to develop a complimentary approach to rainbowlike phenomena, based on Regge poles rather than the classical paths.

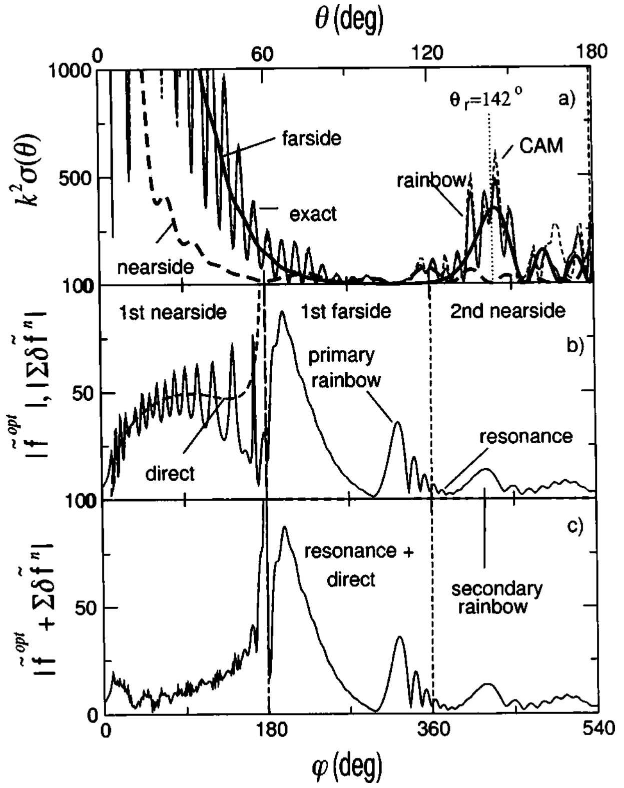

FIG. 6. (a) DCS's for a rectangular potential well with $kR=39$ and refractive index equal to that of water ($N=1.33$): exact (solid) and obtained by the CAM approach (dashed). The rainbow region starts at $\theta \approx 120°$. Also shown are the nearside (thick dashed) and farside (thick solid) components of the DCS. (b) The first and second nearside and the first farside components of the LCF $\Sigma_n \delta\tilde{f}^n(\varphi)$ (solid) and the direct part $\tilde{f}^{opt}(\varphi)$ (dashed) for the same model (ignoring diffraction effects of the potential well). (c) Coherent sum of $\tilde{f}^{opt}(\varphi)$ and $\Sigma_n \delta\tilde{f}^0(\varphi)$.

For $kR \gg 1$, the effective potential combining the rectangular well Eq. (32) with a centrifugal barrier $(\lambda^2 - 1/4)/r^2$ [see the inset in Fig. 7(b)] supports a large number of metastable levels [20,24]. Accordingly, the S-matrix element ($'$ denotes differentiation with respect to the argument)

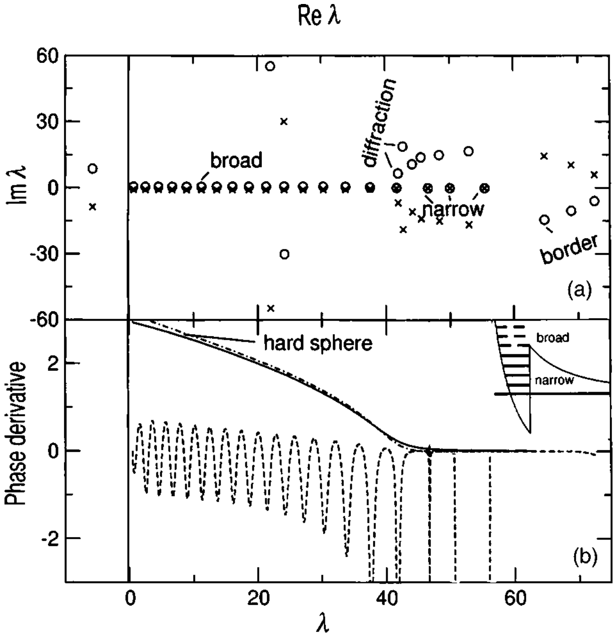

FIG. 7. (a) Poles (circles) and zeroes (crosses) obtained by Padé reconstruction for the rainbow with $kR=39$ and $N=1.33$. Poles corresponding to the narrow (inset, solid) and broad (inset, dashed) resonances are indicated. Inset: schematic diagram showing the metastable states in a combination of the rectangular well and centrifugal potentials; (b) derivative of the phase of the same S-matrix element (solid) and the smooth deflection function (dashed). Also shown for comparison (dot-dashed) is the derivative for the matrix element for a hard sphere of the same radius.

$$S(\lambda) = - \frac{H_\lambda^{2'}(kR)J_\lambda(k_1R) - NH_\lambda^2(kR)J_\lambda(k_1R)}{H_\lambda^{1'}(kR)J_\lambda(k_1R) - NH_\lambda^1(kR)J_\lambda(k_1R)}, \quad N \equiv k_1/k \tag{33}$$

($k \equiv (2mE)^{1/2}, k_1 \equiv [2m(E-V_0)]^{1/2}$, and $J_\lambda(z)$ is the Bessel function of the first kind [23]**)** has a number of resonance Regge poles. The poles arise from the zeroes of the denominator of Eq. (33) and are usually divided into narrow and broad resonances [20,24] which exist below and above the centrifugal barrier, respectively. The poles of the third kind are associated with diffraction (surface waves) on the outer edge of the potential well [24]. We can therefore proceed with the analysis of rainbow scattering as in Sec. IV, allowing for several, rather than just one, LCF terms in Eq. (20). The pole/zero structure for a potential well $kR=39$ and $N=1.33$ (equal to the refraction index of water [24]) obtained with the help of $[31/31]$ Padé approximant is shown in Fig. 7(a). Figure 7(a) shows a total of 19 broad and narrow resonances located just above the real λ axis and two of the diffraction poles near $\lambda \approx 39$. The rest of the available poles form a boundary broadly similar to the one discussed in Sec. IV. The broad resonances strongly affect the derivative of the phase of the S-matrix element as shown in Fig. 7(b) (dashed). The derivative of the potential phase in Eq. (11) obtained after separating the 19 pole terms is shown in Fig. 7(b) by a solid line. The deflection function is similar to that for a hard impenetrable sphere of the same radius, also shown in Fig. 7(b) for comparison (dot-dashed). This illustrates the mixed nature of our CAM representation: the optical term $\tilde{f}^{opt}(\varphi)$ describes nearside trajectories scattered off the edge of the potential in the inset of Fig. 7(a). The effect of those trajectories which penetrate the potential well is described in terms of capture in decaying Regge states. In this language, the farside and remaining nearside regions are accessible via resonance pathways only. A coherent sum of 19 resonance terms, $\Sigma_{n=0}^{18}\delta\tilde{f}^{(n)}(\varphi)$ is shown in Fig. 6(b) (solid).

The resonance part of the unfolded amplitude has a structured nearside component and a large forward scattering peak in the first nearside region. It is followed by clearly resolved oscillations of the primary rainbow structure ($\varphi_r^{prim} \approx 322°$) which extend into the second nearside region. These are, in turn, followed by a weaker secondary Airy structure ($\varphi_r^{sec} \approx 322°$). Thus, in terms of Regge representation Eq. (20), emergence of the rainbow structures in the unfolded amplitude and the DCS is an interference effect involving exponential angular decay of many Regge states supported by the effective potential. This is somewhat similar to the "weak" measurement effect well known in quantum measurement theory. When applied to measure a variable with a spectrum A_n, a weak von Neumann meter with a broad initial state $G(f)$ can produce a reading well away from the region Ξ containing all A_i [25,26], because a coherent sum of $G(f-A_n)$ peaked around A_i may peak outside Ξ. Similarly, a coherent sum of $\delta\tilde{f}^n(\varphi)$ each centered at $\varphi_{res}^n < \pi$ produces the primary rainbow peak in the first nearside region $\pi < \varphi < 2\pi$, as well as the secondary rainbow structure in the second nearside region, etc. As shown in Fig. 6(c), destructive interference between the $\tilde{f}^{opt}$ and the resonance terms reduces the first nearside components of $\tilde{f}$. The semiclassical DCS obtained by folding $\tilde{f}(\varphi)$ [Fig. 6(a), dashed] is in fair agreement with the exact DCS (thin solid). Some discrepancy occurs at large θ due to the fact that our description of resonance scattering becomes inaccurate for poles with small φ_{res}. We note that an equivalent semiclassical description in terms of classical paths can be obtained if we replace in Eq. (9) $S(\lambda)$ by its Debye expansion [24] and evaluate the integrals with the help of the stationary phase approximation. However, if the analytic form of the S-matrix element is unknown, a CAM analysis could be the only option available.

VII. REACTIVE THRESHOLDS AND THE THRESHOLD-INDUCED GLORY

The threshold model analyzed in this section has recently been discussed in connection with the enhanced small angle scattering and time delay observed in the benchmark $H+D_2 \rightarrow HD+D$ reaction and its isotopomers [6,27]. The classical explanation of these effects is as follows [27]. If the energy of the reactants is close to the adiabatic barrier top, the motion along the reaction coordinate is slowed down giving the collision partners time to rotate towards smaller scattering angles. This behavior can be mimicked in a model consisting of an Eckart barrier [15]

$$V(s) = W_0/\cosh^2(s/s_0),$$

where s is the reaction coordinate. The centrifugal potential is chosen to be nearly constant in the vicinity of the barrier top, adding to the potential a constant term $B(\lambda^2-1/4)$, where B is the rotational constant. Thus the S-matrix element is given by the product of the barrier transmission amplitude T [28] and an additional potential phase ϕ, which, as discussed in Sec. V, can be chosen quadratic in λ,

$$S(E,\lambda) = C\,\exp(i\Phi)T(E,\lambda), \tag{34}$$

$$T(E,\lambda) \equiv \frac{\Gamma(-ik+iq+1/2)\Gamma(-ik-iq+1/2)}{\Gamma(-ik)\Gamma(1-ik)}, \tag{35}$$

$$\Phi(\lambda) = a\lambda^2 + b\lambda, \quad a < 0, \tag{36}$$

where

$$k(\lambda)^2 = \epsilon^{-1}[E - B(\lambda^2 - 1/4)], \tag{37}$$

$$q \equiv (W_0/\epsilon - 1/4)^{1/2}, \tag{38}$$

$$\epsilon \equiv \hbar^2/2\mu s_0^2, \tag{39}$$

μ is the reduced mass, $\Gamma(z)$ is the Gamma function [23], and C is an arbitrary constant.

Defined in this way, $S(E,\lambda)$ has simple analytical properties. Its complex energy poles are well studied (see, for example, Refs. [29] and [30]). For $J=0$, $S^{J=0}(E)$ is single valued in the complex E plane cut along the positive real axis. On the second Riemann sheet, the poles $E_n^{J=0}, n=0,1,2\ldots$ of $\Gamma(-ik+iq+1/2)$ given by

$$E_n^{J=0}/\epsilon = [q - i(n+1/2)]^2, \quad n = 0,1,2\ldots \tag{40}$$

correspond to the quasistationary states near the barrier top. These poles form an infinite sequence along the parabola $E_1=q^2-E_2^2/4q^2, E/\epsilon=E_1+iE_2$, which approaches the real axis at $E\approx W_0-\epsilon/4$. For a broad barrier, $W_0/\epsilon \gg 1$, the first few poles lie along the line perpendicular to the real axis, and retaining the leading terms in Eq. (40) yields [29,30]

$$E_n^{J=0} \approx W_0 - 2i\epsilon^{1/2}W_0^{1/2}(n+1/2), \quad n = 0,1,2\ldots. \tag{41}$$

Equations (34) and (37) also show that for a given E, $S(E,\lambda)$ is analytic in the complex λ plane cut from $\pm\lambda_{max}$, where initial translational energy of the system vanishes, $k^2(\lambda_{max})=0$,

$$\lambda_{max} \equiv [B^{-1}E + 1/4]^{1/2}. \tag{42}$$

The first and the second Gamma functions in the numerator of Eq. (34) contribute poles in the first and third quadrants of the first Riemann sheet, and the second and fourth quadrants of the second sheet, respectively. Regge poles in the first quadrant of the first Riemann sheet, which affect the DCS most, are found with the help of the J-shifting condition

$$E - B(\lambda_n^2 - 1/4) = E_n^{J=0}, \quad n = 0,1,2\ldots, \tag{43}$$

with $E_n^{J=0}$ given by Eq. (40). The poles form an infinite string along the line $\lambda_1^2-\lambda_2^2-B(\lambda_1\lambda_2)^2/q^2=(E-q^2)/B+1/4$; $\lambda=\lambda_1+i\lambda_2$. The line starts at the right angle near $\lambda\approx\lambda_B$,

$$\lambda_B \equiv [B^{-1}(E - W_0) + 1/4]^{1/2}, \tag{44}$$

where initial translational energy equals the barrier height, $k^2(\lambda_B)=W_0/\epsilon$. It then bends to the right and eventually runs parallel to the real axis at $\lambda_2=q/B^{1/2}$. For a broad barrier, one has [19]

$$\lambda_n \approx \lambda_B + i(n+1/2)/\theta_0, \tag{45}$$

where

$$\theta_0 \equiv (2\mu)^{1/2}Bs_0\lambda_B/\hbar W_0^{1/2}. \tag{46}$$

Finally, as E increases from zero, the nth pole λ_n follows the Regge trajectory [18] $\lambda_2=\epsilon q(n+1/2)/B\lambda_1$.

Consider next the angular distribution for the J-shifted Eckart model just described. It can be obtained with the help of Eq. (2) where the sum over partial waves is restricted to the open channels, $k^2(\lambda)>0$. For our semiclassical treatment we shall require $\lambda_{max}\gg 1$, $\lambda_B\gg 1$ and $\lambda_{max}-\lambda_B\gg 1$. The DCS for the model specified by the parameters $(C=0.03)$

$$\lambda_B = 25 \quad \lambda_{max} = 43, \quad \theta_0 = 0.25, \quad a = -\pi/60, \quad \text{and} \quad b = \pi \tag{47}$$

is shown in Fig. 8(a). For small θ, it exhibits a pronounced oscillatory structure associated, as discussed above, with the time delay experienced by the partial waves with $\lambda\approx\lambda_B$ near the barrier top. Our aim is to relate this structure to the Regge poles Eq. (43).

As before, we will assume that the numerical values of the S-matrix element are available for a number of physical angular momenta sufficient to converge the PWS Eq. (2). Thus for the model (47) we use the first 35 partial waves to construct a $[17/17]$ Padé approximant. The resulting pole /zero structure with the first four poles of the barrier sequence (closed circles) reproduced correctly and a characteristic “border” defining the region of validity is shown in Fig. 9(a). The derivative of the phase of the S-matrix element (dashed) and the smooth deflection function (solid) obtained after removal of the three leading poles, $(N_{res}=2)$, are shown in Fig. 6(b).

We note first that the combined effect of the poles forces $\{\mathrm{Arg}S(\lambda)\}_\lambda$ below the real axis at the glory angular momentum, $\lambda_{gl}\approx 24$, and it remains negative thereafter. This behavior is indicative of a glory effect [15,28,31], and for sufficiently small angles we may use the glory approximation for the DCS [19,28],

$$\sigma^{gl}(\theta) = 2/\pi(|\Psi_{\lambda\lambda}|k_i^2)^{-1}\lambda_{gl}^2|S(E,\lambda_{gl})|^2|J_0(\lambda_{gl}\theta)|^2, \tag{48}$$

where $\Psi_{\lambda\lambda}$ is the second derivative of the phase $\Psi \equiv \mathrm{Arg}S(\lambda)$. For the Eckart model Eq. (47) a numerical evaluation gives $\lambda_{gl}=23.7$; $|\Psi_{\lambda\lambda}|=0.028$; $|S(E,\lambda_{gl})|=0.26$, and the corresponding glory DCS plotted in Fig. 8(a) by a dashed line is in good agreement with the exact one in the small angle region.

This glory effect is clearly induced by the barrier threshold and can equivalently be described in terms of capture in a number of barrier Regge states. Proceeding as in Secs. II and III, we obtain the optical part, $\tilde{f}^{opt}$ and the first three

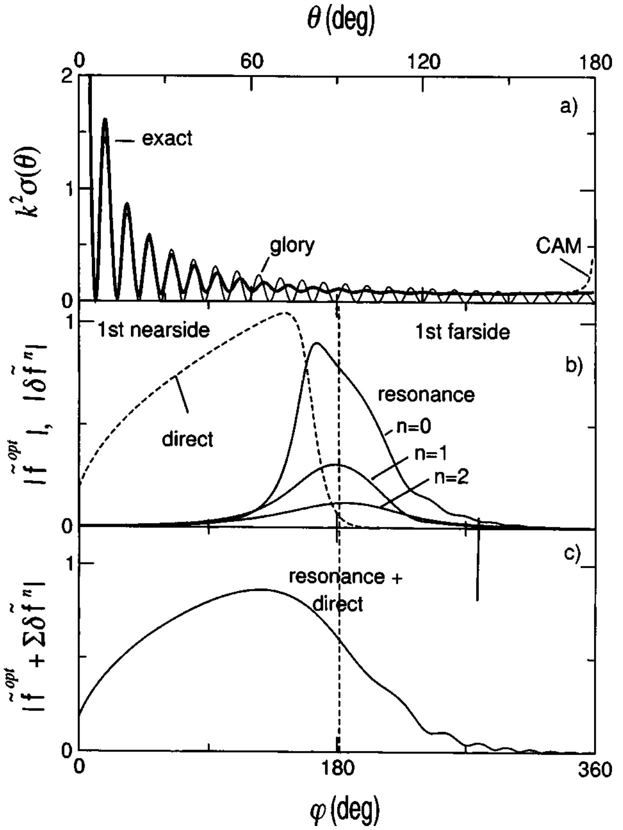

FIG. 8. DCS's for the Eckart threshold model with parameters given in Eq. (47). (a) exact (thick solid), obtained by CAM approach (dashed) and the glory approximation Eq. (48) (thin solid). (b) The first nearside and farside components of the LCF $\widetilde{\delta f}^{n}(\varphi), n=0,1,2$ and the direct component $\tilde{f}^{opt}(\varphi)$ for the above model; (c) coherent sum of $\tilde{f}^{opt}(\varphi)$ and $\Sigma_{n=0}^{2}\widetilde{\delta f}^{0}(\varphi)$.

LCF's, $\widetilde{\delta f}^{n}$, $n=0,1,2$ for the unfolded amplitude $\tilde{f}(\varphi)$ which are shown in Fig. 8(b). The optical part $\tilde{f}^{opt}(\varphi)$ is contained within the first nearside region. The LCF's, describing the capture in the first three Regge states associated with the barrier top, rapidly decrease in magnitude as n increases. Although their angular lives are short, they have φ_{res}^{n} close to 180° and extend into the first farside region. The coherent sum of all four terms in Fig. 8(c) is smooth and contains considerable first nearside and farside components. Thus the small angle oscillations in Fig. 8 have a nearside-farside origin and can be seen to result from the barrier top resonance. We note that the short angular lives of the barrier Regge states prevent us from relating $\tilde{f}^{opt}$ to a particular class of classical trajectories, the way it has been done in Secs. IV and VI. Nevertheless, the CAM analysis, in its general form, successfully describes the glory effects in reactive collisions [15].

VIII. DISCUSSION AND CONCLUSIONS

In summary, we have found that the semiclassical CAM approach outlined in Secs. II and III provides a convenient procedure for analyzing angular scattering by a range of potentials possessing one or several significant Regge poles. In doing so, it decomposes the scattering amplitude $\tilde{f}$ into (usually nearside) "direct" component $\tilde{f}^{opt}$ and the correction term $\widetilde{\delta f}$ associated with the poles which are not correctly described by the primitive semiclassical approximation. The correction term can extend beyond the first nearside region and is often responsible for nearside-farside oscillatory pattern observed in the DCS's. The meaning of the two terms and, in particular, their relation to the classical trajectories varies with the model analyzed. Thus for the single resonance case in Secs. IV and V the optical part comprises all trajectories reflected by the outer sphere and is consistent with the result one would obtain in a classical trajectories simulation. The LCF term, on the other hand, contains effects of tunneling and cannot be described in terms of classical trajectories. This changes when one considers the optical rainbow of Sec. V. There the optical part contains only the trajectories reflected by the edge of the potential well and are similar to those scattered off an impenetrable sphere. The correction term, on the other hand, contains contributions which can equivalently be described in terms of paths penetrating the interior of the well. A different semiclassical representation, e.g., based on the Debye expansion [24], could help redefine it in terms of such paths rather than resonances. The relation between $\tilde{f}^{opt}$ and the classical paths becomes even more vague for the threshold model of Sec. VII. Nevertheless, in this case, the LCF retains its meaning of a correction arising from, however short, capture in the barrier states. It is therefore broadly consistent with the picture of reactants rotating further while being detained near the barrier top. Spectacular enhancement of small angle scattering is

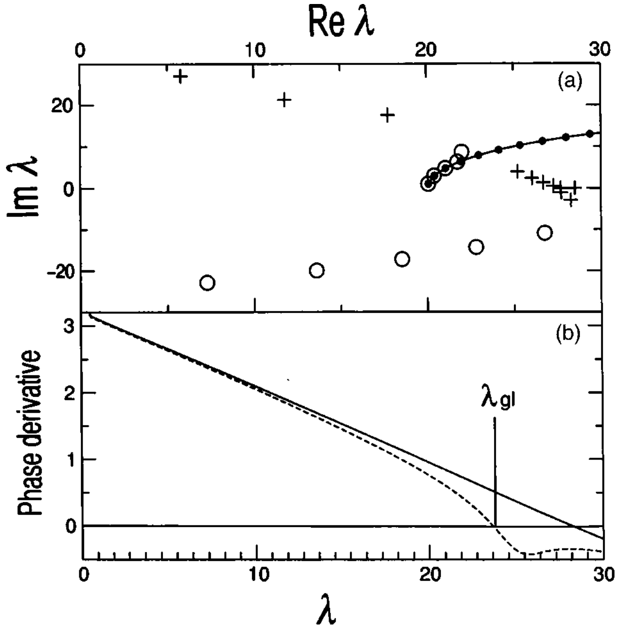

FIG. 9. (a) Poles (circles) and zeroes (crosses) obtained by Padé reconstruction for the Eckart threshold model with parameters given by Eq. (47). Also shown (joined closed circles) are the exact barrier poles. (b) Derivative of the phase of the same S-matrix element (solid) and the smooth deflection function (dashed).

due to the fact that since the captures occur for large impact parameters, the reactants do not have to rotate far to enter the first farside region and cause nearside-farside oscillations. In this region, the combined effect of the barrier poles can alternatively be described as a threshold-induced glory. In short, the present CAM approach is seen as complimentary to other, sometimes more straightforward, techniques developed to describe semiclassical angular scattering. It should be noted, however, that in a situation where a realistic *S*-matrix element has been evaluated numerically, the CAM method may be the only practical tool for such an analysis.

We conclude with a few remarks about the Padé reconstruction. As discussed in Ref. [12], the poles of a Padé approximant fall into three categories: the true poles of the *S*-matrix element, those forming the Froissart doublets, and the background poles. The Froissart doublets mimic rapid noiselike variation of $S(\lambda)$ on the real axis and usually lie close to the axis. Their number increases with the amount of nonanalytical noise contained in the input values of $S(\lambda)$. It is the behavior of the background poles that we found most interesting. For low levels of noise (high accuracy data) they form a well-defined border around the subset of the complex plane where the Padé approximant reproduces $S(\lambda)$ and therefore its true poles correctly. Beyond the boundary, the approximant fails. The role of the finite number of border poles is to imitate the effect of an infinite number of true (in our case, diffraction) poles within a finite region of the complex plane. The border poles are unstable with respect to a change in the input data or the level of noise. In particular, adding a larger amount of nonanalytical noise to the input causes the border to shrink (Fig. 3). The fact that the border poles are nonphysical does not restrict the validity of the CAM representation Eq. (20) as long as only the true physical poles are included into the LCF terms. Indeed, in this case, the border poles contribute to only the direct part $\tilde{f}^{opt}$ which itself is computed by applying the stationary phase method on the real λ axis and does not rely on any reference to the pole positions. It can, however, happen [15] that the accuracy of the input data is such that the approximant fails to reproduce some of the true poles (in the case of Ref. [15], threshold poles with $n>0$) whose LCF's are needed in order to reproduce the DCS to a sufficient accuracy. If so, several background poles λ_n may occur close to a physical pole and their corrections $\widetilde{\delta f}^n$ can be included in Eq. (20). It has been shown [15] that even though some of the individual terms $\widetilde{\delta f}^n$ would be wrong, their coherent sum $\Sigma_n \widetilde{\delta f}^n$ is correct. In this case, the method describes the combined effect of all poles without resolving individual Regge states. Since the quality of the scattering data obtained in numerical simulations of realistic systems is usually not very high (an error of $\approx 5-10\%$), it seems reasonable to depart from the usual practice of trying to compute individual Regge pole and residues to a very high accuracy [18], and to concentrate instead on the general shape of pole/zero configurations and evaluation of the corresponding semiclassical asymptotes to the scattering amplitude. To this end, we found it sufficient to use in our calculations the normal machine, rather than multiple precision, suggested in Ref. [12]. Also, the elaborate preconditioning procedure described in Sec. II of Ref. [16] appears, in most cases, unnecessary and a simple removal of a part of the potential phase as described by Eq. (23) can be used instead. A more detailed study of the use of the Padé approximation for analytical continuation of *S*-matrix elements will be given in our future work.

ACKNOWLEDGMENTS

One of us (D.S.) gratefully acknowledges the support by the EPSRC (UK), Grant No. GR/S03799/01 and by the CTSPS, Clark Atlanta University, as well as the kind assistance of Professor Ray Flannery. Discussions with Dr. Daniel Bessis are appreciated. A.Z.M. was supported by the U.S. DOE, Division of Chemical Sciences, Office of Basic Research.

[1] W. H. Miller, Adv. Chem. Phys. **25**, 69 (1974).
[2] T. Yamamoto and W. H. Miller, J. Chem. Phys. **118**, 2335 (2003).
[3] Y. Zhao and W. H. Miller, J. Chem. Phys. **118**, 9605 (2002).
[4] T. Yamamoto, H. Wang, and W. H. Miller, J. Chem. Phys. **116**, 7335 (2002).
[5] D. Skouteris, J. F. Castillo, and D. E. Manolopoulos, Comput. Phys. Commun. **133**, 128 (2000).
[6] S. C. Althorpe, F. Fernández-Alonso, B. D. Bean, J. D. Ayers, A. E. Pomerantz, R. N. Zare, and E. Wrede, Nature (London) **416**, 67 (2002).
[7] D. Sokolovski, J. N.L. Connor, and G. C. Schatz, Chem. Phys. Lett. **238**, 127 (1995).
[8] D. Sokolovski, J. N. L. Connor, and G. C. Schatz, J. Chem. Phys. **103**, 5979 (1995).
[9] D. Sokolovski, J. F. Castillo, and C. Tully, Chem. Phys. Lett. **313**, 225 (1999).
[10] D. Sokolovski, Phys. Rev. A **62**, 024702 (2000).
[11] D. Sokolovski and J. F. Castillo, Phys. Chem. Chem. Phys. **2**, 507 (2000).
[12] D. Vrinceanu, A. Z. Msezane, D. Bessis, J. N. L. Connor, and D. Sokolovski, Chem. Phys. Lett. **324**, 311 (2000).
[13] F. J. Aoiz, L. Bañares, J. F. Castillo, and D. Sokolovski, J. Chem. Phys. **117**, 2546 (2002).
[14] D. Sokolovski, Russ. J. Phys. Chem. **76**, Suppl. 1, 21 (2002).
[15] D. Sokolovski, Chem. Phys. Lett. **370**, 805 (2003).
[16] D. Bessis, A. Hafad, and A. Z. Msezane, Phys. Rev. A **49**, 3366 (1994).
[17] H. J. Korsh and K. E. Thylwe, J. Phys. B **16**, 793 (1983).
[18] J. N.L. Connor, J. Chem. Soc., Faraday Trans. **86**, 1627 (1990).
[19] D. M. Brink, *Semi-classical Methods in Nucleous-Nucleous Scattering* (Cambridge University Press, Cambridge, England, 1985)
[20] H. M. Nussenzveig, *Diffraction Effects in Semiclassical Scattering* (Cambridge University Press, Cambridge, England,

1992)
[21] R. G. Newton, *The Complex j-Plane: Complex Angular Momentum in Non-relativistic Quantum Scattering* (Benjamin, New York, 1964)
[22] L. B. Felsen and M. Marcuvitz, *Radiation and Scattering of Waves* (Prentice-Hall, Englewood Cliffs, NJ, 1973), Chap. 4.4
[23] M. Abramowitz and I. A. Stegun, *Handbook of Mathematical Functions*, Applied Mathematics Series (U.S. GPO, Washington, DC, 1964)
[24] J. A. Adam, Phys. Rep. **356**, 229 (2000).
[25] Y. Aharonov, D. Z. Albert, and L. Vaidman, Phys. Rev. Lett. **60**, 1351 (1988).
[26] Y. Aharonov and L. Vaidman, Phys. Rev. A **41**, 11 (1990).
[27] S. A. Harich, D. Dai, C. C. Wang, X. Yuang, S. D. Chao, and R. T. Skodje, Nature (London) **419**, 281 (2002).
[28] L. D. Landau and E. M. Lifshitz, *Quantum Mechanics*, 3rd ed. (Pergamon, Oxford, 1977)
[29] R. Sadeghi and R. T. Skodje, J. Chem. Phys. **102**, 193 (1995).
[30] R. Sadeghi and R. T. Skodje, Phys. Rev. A **52**, 1996 (1995).
[31] J. N. L. Connor, Phys. Chem. Chem. Phys. **6**, 377 (2004).